Combustion and Flame 242 (2022) 112088

Contents lists available at ScienceDirect

Combustion and Flame

journal homepage: www.elsevier.com/locate/combustflame

Effect of equivalence ratio and temperature on soot formation in partially premixed counterflow flames

Kevin Gleason, Francesco Carbone[1], Alessandro Gomez*

Yale Center for Combustion Studies, Department of Mechanical Engineering and Materials Science, Yale University, 9 Hillhouse Avenue, New Haven, CT 06520-8286, United States

ARTICLE INFO

Article history:
Received 3 November 2021
Revised 27 February 2022
Accepted 27 February 2022
Available online 11 June 2022

Keywords:
Soot
Counterflow
Partially premixed flames

ABSTRACT

Soot formation is quantified in detail (volume fraction, particle size, number concentration, and light emissivity dispersion exponent) in a series of partially premixed counterflow flames of ethylene at equivalence ratios, Φ, equal to 6.5, 5.0, and 4.0, and with maximum temperature spanning approximately 200 K. The focus is to investigate the effect of peak temperature and equivalence ratio on soot formation while maintaining constant global strain and stoichiometric mixture fraction. Oxygen is progressively displaced from the oxidizer to the fuel stream of a diffusion flame to stabilize partially premixed flames of decreasing Φ, showing a double-flame structure consisting of a rich premixed flame component stabilized on the fuel side of the stagnation plane and a diffusion flame component stabilized on the oxidizer side. Soot is detected in the region sandwiched between the two flame components, is formed in both of them, and is convected away radially at the Particle Stagnation Plane (PSP). At fixed Φ, raising the peak temperature invariably raises the soot volume fraction throughout the probed region. Vice versa, at fixed peak temperature, lowering the equivalence ratio causes the premixed flame component to shift away from the diffusion flame component, with the consequent broadening of the soot forming region and an increase in both soot volume fraction as well as soot particle sizes through an enhancement of surface growth. Detailed probing of the region in the vicinity of the PSP offers evidence of soot oxidation from molecular oxygen. Furthermore, when the maximum temperature is sufficiently low, the net soot production rate turns negative because surface oxidation overwhelms surface growth. Comparing the soot *number* production rate inferred from experiments to the dimerization rate of benzene (C_6H_6), naphthalene ($C_{10}H_8$), and pyrene ($C_{16}H_{10}$) reveals that only the smallest aromatics are present in flames at sufficiently large concentrations to account for soot nucleation. This observation applies to both the diffusion flame and the premixed flame components and confirms previous findings in strictly diffusion flames.

1. Introduction

Combustion systems are typically categorized as either premixed or non-premixed (i.e., diffusion), with soot formation being studied separately in either environment, as reviewed in [1–3]. In practical systems, however, situations arise in which these two regimes may coexist. For example, in compression ignition engines, a double-flame structure was suggested with soot forming in fuel-rich premixed conditions before being oxidized in a non-premixed flame [4]. Control and eventual abatement of soot formation under these conditions are critical not only from the perspective of engine performances but also in the context of the negative impact of soot emission on human health [5] and climate change [6]. Therefore, studying the formation of soot in partially premixed flames (PPF), while avoiding the complexity of real engine conditions, is of fundamental and practical interest. The laminar counterflow configuration is ideal for such a task because it allows establishing a one-dimensional dual-flame structure, retaining the coupling of chemistry and transport phenomena, with the sooting region being sandwiched between a premixed flame and a diffusion flame [7].

Efforts to quantify the effect of equivalence ratio [7–13], pressure [14,15], and fuel type [16–19] on PAH, soot, and NOx emissions in partially premixed flames were the object of several studies. The effects of partial premixing are reported to increase the concentration of soot and its precursors in previous studies of our group [7,15], in contrast with the findings of [9,12] reporting that an increase in oxygen and oxidative reactions decrease the concentration of soot precursors. An important difference that

---

* Corresponding author.
E-mail address: alessandro.gomez@yale.edu (A. Gomez).

[1] Current Address: Department of Mechanical Engineering, University of Connecticut, 191 Auditorium Road, Unit 3139, Storrs, CT 06269-3139, USA

https://doi.org/10.1016/j.combustflame.2022.112088

explains the discrepancy between the two types of investigations is that partial premixing in [7,15] is implemented under conditions of constant stoichiometric mixture fraction, requiring the shift of oxygen from the oxidizer stream to the fuel steam to control the level of premixing. Holding the stoichiometric mixture fraction constant ensures that the location of the diffusion flame component is fixed and allows for the isolation of the effects of partial premixing on soot formation [11,12]. The fuel type must also be taken into consideration as the effect of partial premixing on soot emissions in ethylene flames may differ compared to propane [17] and methane [12] ones. To isolate the effect of the equivalence ratio, one can keep the diffusion (non-premixed) flame component invariant to the changes in oxygen concentration in the fuel stream, which is easily realizable in the counterflow configuration.

Another key parameter in soot formation is temperature. Several studies focused on the effect of temperature in diffusion flames [20–22] and premixed flames [23,24]. It is not surprising that in counterflow diffusion flames, an increase in flame temperature increases soot volume fraction because soot oxidation is often negligible when the flame is positioned on the oxidizer side of the stagnation plane. In premixed flames, the effect of temperature on soot load can be non-monotonic as oxidation reactions decrease the concentration of precursors [23]. In view of the different trends in the two separate flame environments, understanding the effect of temperature in partially premixed flames, where both flame components are present, is of interest. The effect of temperature in partially premixed coflow flames were investigated in [25], using different diluents (Ar, N_2, and CO_2) to control temperature. However, as reported in [21], the effect of inert dilution in diffusion flames can be comparable or even larger than the temperature effect, and CO_2 dilution can introduce additional chemical effects, so it is ideal to isolate the effect of temperature by other means. Following the method of [22], one can investigate the effect of temperature in detail by keeping constant equivalence ratio, global strain rate, and stoichiometric mixture fraction.

Generally, there remains a lack of information on the crucial step of particle inception [3] even in the much more extensively studied diffusion flames and premixed flames, let alone the PPFs under consideration. To follow the relevant gas-to-particle transition, gaseous sampling is virtually indispensable for the complete chemical characterization of the flame environment up to multiring aromatics [26]. Since the presence of soot and ensuing probe clogging poses challenges to microprobe sampling, lightly sooting conditions are typically established. Here we study soot formation beyond the lightly sooting conditions by perturbing the investigated flames in a highly controlled manner [22,27]. In a previous study [7] we investigated a lightly sooting flame by quantifying gaseous species up to three-ring aromatics to validate a chemistry model in predicting temperature and important soot precursors (e.g., acetylene and benzene). Now, we perturb the flame slightly to vary the soot load and rely on the validated kinetic model to predict the structure of the flame under perturbed conditions. The level of inert dilution is selected to keep constant global strain rate and stoichiometric mixture fraction, while adjusting the maximum flame temperature in increments of approximately 50 K. The study allows highlighting the effects of flame temperature and equivalence ratio on soot formation in as controlled a fashion as possible.

2. Experimental and computational methods

2.1. Boundary conditions, flame selection criteria, and key flame properties

Experiments are performed using a burner consisting of two opposed converging nozzles, 8 mm apart, with a 6.35 mm internal diameter outlet. Both nozzles are surrounded by conical enclosures conveying a nitrogen shroud flow to minimize external disturbances to the flame. Further details regarding the burner geometry are in [28]. Calibrated flows of nitrogen/ethylene/oxygen and nitrogen/oxygen are fed to the bottom and top nozzles, respectively, to stabilize PPFs at atmospheric pressure. The mass averaged velocity (at a reference lab temperature of 298 K) is fixed at 19.8 cm/s and 21.2 cm/s for the fuel and oxidizer streams, respectively, resulting in a global strain rate of $50s^{-1}$. One-dimensional modeling of the flames is performed with ANSYS CHEMKIN-Pro [29] and the most recent version of the soot model made available online by the group in Milan (C1-C16 HT SOOT, mechanism Version 2003, March 2020). This mechanism considers 452 species and 24,041 reactions [30,31] and includes 80 pseudo species 'BINs' composed of 20 up to 10^8 carbon atoms to model soot, as described in [32]. We account for multicomponent diffusion coefficients, thermal diffusion, and thermal radiation of CO, CO_2, H_2O, and CH_4 in the optically thin limit [33]. Soot radiation is estimated to be insignificant in these flames based on Dalzell and Sarofim [22,34]. A 2-D axisymmetric model using COMSOL multiphysics is applied to account for deviation from ideal plug flow boundary conditions, as in [7]. This model estimates the centerline velocity and its axial gradient (27.8 cm/s and $52.9s^{-1}$ for the fuel stream and 34.1 cm/s and $32.4s^{-1}$ for the oxidizer stream, respectively) for a pure diffusion flame whose perturbation leads to the PPFs investigated in this study. The expected variations of the actual velocity and velocity gradients at the burner nozzle caused by the imposed perturbation of the flame temperature and equivalence ratio are neglected.

The mole fraction boundary conditions of the investigated flames at three equivalence ratios, Φ, are reported in Table 1 with bold entries highlighting the two flames that had been characterized comprehensively in [7] by measuring flame temperature and mole fraction profiles of over 30 gaseous species. These measurements were used to validate the computational chemical kinetic model with respect to some important variables in soot formation such as temperature, acetylene, and benzene concentrations, and build confidence in its predictive capability under the present conditions of modest perturbations in peak temperature of the validated flames.

With an approach similar to [22,27], flames are selected to study the effect of temperature and equivalence ratio on soot formation by perturbing the mass fraction of ethylene in the fuel stream at constant stoichiometric mixture fraction, $Z_{st} = 0.183$. For partially premixed flames, $Z_{st} = (1 + s\ Y_{rF}/Y_{OO})^{-1}$ where $Y_{rF} = Y_{FF}(1 - 1/\Phi)$ is assumed to be the mass fraction of the *residual* fuel assuming complete conversion to CO_2 and H_2O from the premixed flame (PF) component. The constancy of Z_{st} and mass averaged velocities (i.e., strain rate) ensures that the relative position of the diffusion flame component with respect to the stagnation plane is approximately constant, and therefore the perturbation in mass fraction of fuel is primarily used to tune T_{max} in increments of approximately 50 K. The approach allowed us to vary T_{max} at constant Φ, spanning a range of approximately ∼200 K. The range is limited to ∼150 K for the flames with Φ=4.0 because of their sensitivity of soot load to temperature.

2.2. Soot pyrometry

Soot measurements are performed using two-color pyrometry, as extensively detailed in [22,35,36] and only briefly covered hereafter. Soot luminosity is measured by acquiring flame images with a CCD camera (Nikon D70). The images are captured with a 210 mm focal length lens using a 550 nm long-pass filter so that only the red and green channels of the camera are used for further processing. The long-pass filter is used to remove some of

Table 1
Boundary conditions in mole fraction and computed maximum flame temperature, T_{max}, for all investigated flames at three equivalence ratios, Φ. The stoichiometric mixture fraction is held constant at Z_{st} = 0.183. Flames whose gas-phase composition was characterized experimentally in [7] are shown in bold, whereas flames reported in italic are 'soot-free' with respect to the detectable Rayleigh scattering signal.

		Fuel Stream ($T = 298$ K)			*Oxidizer Stream* ($T = 323$ K)	
	T_{max} (K)	C_2H_4	N_2	O_2	N_2	O_2
Φ=6.5	*1920*	*0.3000*	*0.5615*	*0.1385*	*0.8287*	*0.1713*
	1955	**0.3100**	**0.5469**	**0.1431**	**0.8230**	**0.1770**
	2007	0.3250	0.5250	0.1500	0.8144	0.1856
	2056	0.3400	0.5031	0.1569	0.8058	0.1942
	2104	0.3550	0.4812	0.1639	0.7972	0.2028
Φ=5.0	*1866*	*0.2800*	*0.5520*	*0.1680*	*0.8499*	*0.1501*
	1904	0.2900	0.5360	0.1740	0.8446	0.1554
	1941	**0.3000**	**0.5200**	**0.1800**	**0.8392**	**0.1608**
	2012	0.3200	0.4880	0.1920	0.8285	0.1715
	2064	0.3350	0.4640	0.2010	0.8205	0.1795
Φ=4.0	*1819*	*0.2600*	*0.5450*	*0.1950*	*0.8702*	*0.1298*
	1860	0.2700	0.5275	0.2025	0.8652	0.1348
	1900	0.2800	0.5100	0.2100	0.8603	0.1397
	1961	0.2950	0.4838	0.2213	0.8529	0.1471

the chemiluminescence signals from the two flame fronts. The lens aperture is set at f/8 and mounted on extension tubes to provide a magnification of 15.6 μm/pixel. Images are captured in a 12-bit lossless (raw) format and averaged over 20 samples. They are split into individual red, green, and blue color channels and deconstructed into a 2D projection using an Abel transform.

The ratio of the two deconvoluted color channels, S, is described by the ratio of the radiation intensity emitted according to Planck's law

$$\frac{S_g}{S_r} = \frac{\int \eta_g(\lambda)\,\lambda^{-(5+\alpha)}\left[\exp\left(\frac{hc}{\lambda k_B T}\right)-1\right]^{-1} d\lambda}{\int \eta_r(\lambda)\,\lambda^{-(5+\alpha)}\left[\exp\left(\frac{hc}{\lambda k_B T}\right)-1\right]^{-1} d\lambda}, \tag{1}$$

where λ, h, c, and k_B are the wavelength, Planck constant, speed of light, and Boltzmann constant, respectively. The subscripts *r* and *g* represent the red and green channels of the camera, respectively. The sensor detection efficiency and transmission losses through the camera lens and the long-pass filter are accounted for in $\eta(\lambda)$, resulting in measurements collected over an approximate spectral range of 550 nm to 700 nm. Eq. (1) substitutes the emissivity of soot particles with an assumed power-law dependence $\varepsilon(\lambda) \propto \lambda^{-\alpha}$ [22,36], where α is referred to as the dispersion exponent. Considering that the dispersion exponent is far from constant in flames, especially under incipiently sooting conditions [22,36,37], we use the computed temperature profile in Eq. (1) to infer the profiles of the dispersion exponent [22]. The dispersion exponent is not only an important optical parameter describing the wavelength dependence of the extinction coefficient [37], but also gives a rough indication of the soot age, since it is related to the particle Hydrogen/Carbon (H/C) content [38].

The computed temperature profile is also used to extract the soot volume fraction through

$$f_v = -\frac{\lambda_e}{\tilde{K}_{ext} L_p} \ln\left\{1-\epsilon_{ref}(\lambda_e)\frac{\tau_{ref}S_{soot}}{\tau_{soot}S_{ref}}\exp\left[-\frac{hc}{k_B\lambda_e}\left(\frac{1}{T_{ref}}-\frac{1}{T_{soot}}\right)\right]\right\}, \tag{2}$$

where λ_e is the effective channel wavelength, L_p the pixel length, and τ the exposure time [39]. The subscript *soot* refers to the measured soot particles and *ref* refers to an absolute light calibration, that was generated using an S-type thermocouple [40]. The dimensionless extinction coefficient is assumed to be $\tilde{K}_{ext} = 5.34 \pm 2.68$ for all flames [22]; the uncertainty lumps the variability of the extinction coefficient to soot morphology and composition and the general uncertainty of the absorption function E(m) [41]. Error bars in the reported measurements of the dispersion exponent and the soot volume fraction represent the 95% confidence of the overall uncertainty in the measurements, including the uncertainty in measured color ratio, the emissivity of the calibrating thermocouple, the measured temperature, the extinction coefficient, and an estimate of the transmission efficiency of the camera and the entire optical lensing system.

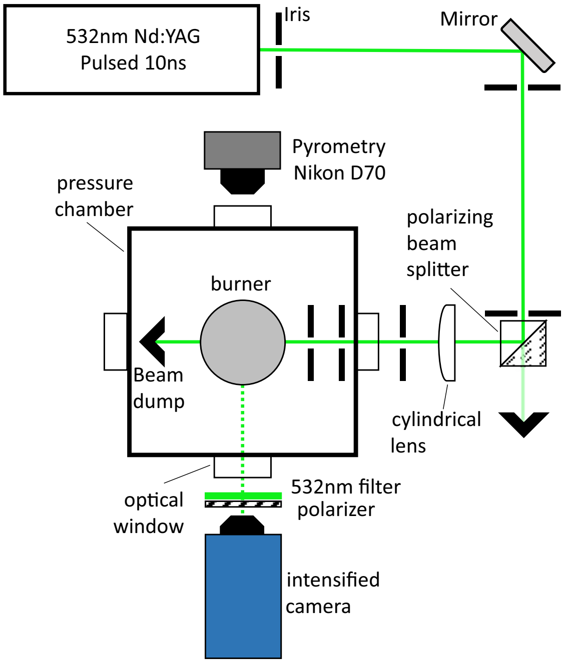

Fig. 1. Experimental layout for soot pyrometry and laser light scattering.

2.3. Light scattering

Planar light scattering measurements are performed with the (532 nm) second harmonic of a 10 ns pulsed Nd:YAG laser (New Wave Gemini PIV). The experimental layout is shown in Fig. 1. A cylindrical lens shapes the laser beam into a 4 mm by 1 mm sheet at the center of the burner with the laser fluence kept below 100mJ/cm^2 to ensure that soot particles are neither significantly overheated nor ablated by the high energy pulses [42], as verified experimentally. The scattered light is imaged onto an intensified camera (12-bit PCO DiCAM-Pro) positioned at a 90° scattering angle, through an optical train including an 80 mm macro lens, a polarizer, and a 532nm±10 nm interference filter. Data analysis is performed on the average of 500 images captured in a 20 ns gating window centered around the triggering of the laser pulse. Background subtraction is applied by imaging the flame without laser illumination. The gas-phase total light scattering coefficient of the investigated flames is calculated using the computed number concentration of the following gasses: H_2, H_2O, N_2, O_2, CH_4, CO, CO_2, C_2H_2, C_2H_4, C_2H_6, C_3H_8, C_3H_4, C_4H_6, and C_6H_6 whose scattering cross-section are reported in the literature [43–46]. All species accounted for in gas phase scattering, except for H_2O, were measured and quantified with the GC/MS in the fully characterized flames in bold in Table 1. Multiring PAHs whose scattering cross-section is expected to be much larger than that of benzene appear at significantly lower concentrations and contribute negligibly to the overall gas-phase scattering coefficient.

Calibration gasses (propane, ethylene, and nitrogen) are flowed individually through both top and bottom nozzles and imaged onto the intensified camera to verify that the appropriate ratios of the scattering coefficient are obtained. The calibration of any one gas (‘*cal*’) is used to convert the measured Rayleigh signal *S* to the scattering coefficient Q_{vv},

$$Q_{vv} = S_{meas}\frac{NC_{vv}^{cal}}{S_{cal}}, \tag{3}$$

where *N* is the local gas number density and C_{vv} is the scattering section of the calibration gas with the subscript ‘*vv*’ referring to both incident and scattered vertically polarized light. The soot number concentration N_s is evaluated under the hypothesis of size monodispersity as

$$N_s = \frac{9\pi^2 F(m) f_v^2}{Q_{vv}^{soot}\lambda^4}, \tag{4}$$

where Q_{vv}^{soot} is the measured excess scattering coefficient attributed to soot, net of the Rayleigh scattering contribution from the gas phase, f_v is the measured soot volume fraction via pyrometry, and $F(m) = 0.69\pm0.13$ is the dimensionless refractive index function at the laser wavelength $\lambda = 532$ nm based on the relationship between $F(m)$ and the dimensionless extinction coefficient [47]. The assumption of monodispersity in initial particle size leads to underestimate the soot number density. This assumption is reasonable in the zone where particles nucleate (mostly at high temperature downstream of the diffusion flame component) but may become progressively weaker as particles evolve on their path towards the stagnation plane. Nevertheless, the small sizes measured by light scattering should preclude the existence of a large polydispersity in the soot particle population and the soot particle diameter can be safely assumed spherical and evaluated by

$$d = \left(\frac{6 f_v}{\pi N_s}\right)^{1/3}. \tag{5}$$

Error bars in the reported measurements of the soot number concentration and particle size represent the 95% confidence of the overall uncertainty in the measurements, including the uncertainty in measured scattering coefficient, the dimensionless refractive index function, and the soot volume fraction.

3. Results and discussion

3.1. Complementing the database

One of the objectives of the present work is to complement the extensive database of atmospheric partially premixed flames [7] with soot measurements. An overview of the structure of a subset of the examined flames at approximately constant $T_{max} = 1950\,K \pm 11$ K but with different Φs is provided in Fig. 2, comparing measured values from [7] (symbols) with simulations from the CRECK kinetic model (lines). The computed soot profile is the sum of all 80 pseudospecies BINs. The abscissa is the position along the burner axis and is centered at the gas stagnation plane (GSP). Negative values refer to the fuel stream and positive values to the oxidizer one, whereas the vertical solid line marks the particle stagnation plane (PSP) calculated by $V_{th} = -0.538\nu\nabla\ln(T)$ [48], using the temperature gradient and kinematic viscosity (ν) from the model. Results of the model and experiments are overlapped by superimposing the computed maximum concentration of CH* with the maximum chemiluminescence signal of the diffusion flame component in the recorded images. Fig. 2 highlights the evolution from the fuel (ethylene) to aromatics such as benzene (C_6H_6), naphthalene ($C_{10}H_8$), and pyrene ($C_{16}H_{10}$). Pyrene was not quantified experimentally and we provide only the computed profiles. Profiles of oxygen and hydroxyl radical (OH) are also provided with the results of the soot measurements from this work. The model captures well all of the gaseous species, but underpredicts the volume fraction by approximately one order of magnitude. Fig. 2 includes the model predictions for a flame with Φ=4.0 (right panel) that has not been validated via gas phase speciation but is the result of a small perturbation of the boundary conditions of the other validated flames [7]. The existence of a double flame structure consisting of a diffusion flame component, near the peak of OH on the oxidizer side of the GSP, and a premixed flame component on the fuel side, is highlighted by the “shoulder” of the OH profiles at the left of the peak that is most apparent at Φ=4.0 and 5.0, as further discussed below.

To demonstrate the effect of temperature on the flame structure, we show in Fig. 3 the computed temperature, critical species in soot surface reactions (i.e., OH, O_2, and C_2H_2) for all the investigated flames listed in Table 1. The predictive ability of the model should be minimally affected by the perturbation of the boundary conditions to vary Φ and/or T_{max}. Given the discrepancy between the measured volume fraction and computed soot (BIN) profiles in Fig. 2, we focus only on critical gaseous species. As already mentioned, the approach of keeping constant the stoichiometric mixture fraction anchors the position of the diffusion flame component (i.e., the location of T_{max}) relative to the GSP as T_{max} is varied. The premixed flame component is stabilized on the fuel side of the GSP at the position highlighted by the shoulder in the OH profile where the (temperature and Φ-dependent) stretched laminar flame speed matches the local axial velocity. The premixed flame component moves toward the fuel nozzle when one reduces Φ and/or increases T_{max} because of the increased laminar flame speed while the velocity boundary condition is fixed. As a result, the heat released by the premixed flame component progressively broadens the temperature profile at decreasing Φ and increasing T_{max}.

Overall, the increase in T_{max} and the consequent boosting of the laminar flame speed results in a nearly constant increase in temperature throughout the entire soot-forming region of the flames. The acetylene mole fraction peaks at increasingly larger values and closer to the fuel nozzle (left), as T_{max} increases and Φ decreases, while the bulk of hydroxyl radical remains primarily on the oxidizer side of the GSP. The relative concentrations of O_2 and OH and their effect on soot oxidation will be revisited later in the discussion.

We perform Rayleigh light scattering measurements of a nonsooting flame at each Φ to assess the beam steering effects [49] and the accuracy of the implemented diagnostic. There are two main objectives that the Rayleigh scattering measurements address: i) verify that the scattering contribution of the gas phase (Q_{vv}^{gas}) is well predicted and ii) assess the accuracy of the modeled temperature profile in view of the fact that the laminar flame

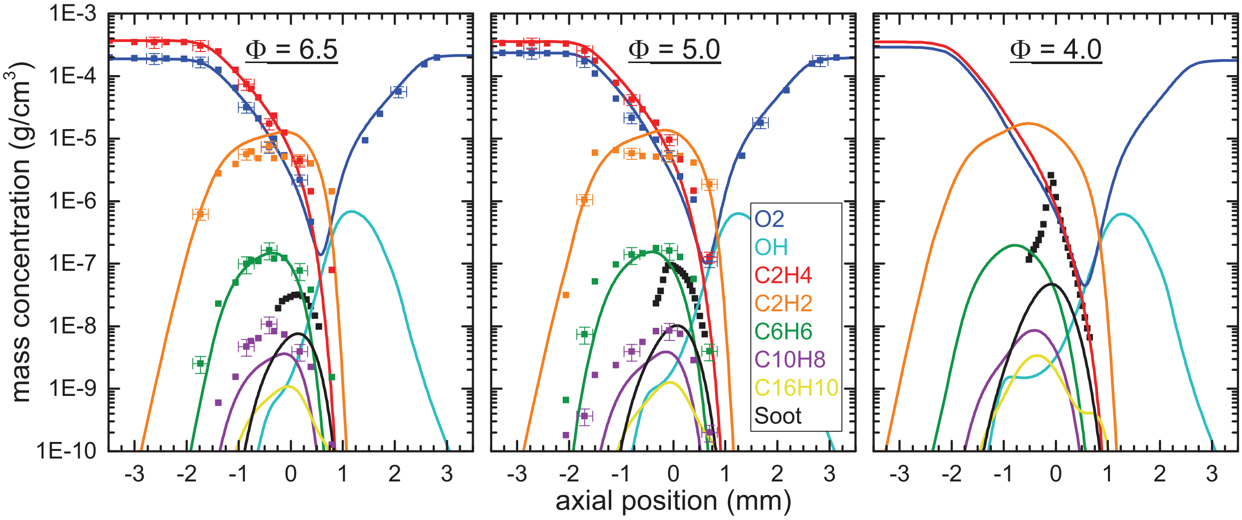

Fig. 2. Profiles of species concentration for flames at Φ=6.5, 5.0, and 4.0 and a nearly constant computed T_{max} =1950 *K* ± 11 K. Gaseous species are taken from [7]. The model [30,31] accounts for soot with 80 pseudospecies 'BINs' whose integrated concentration is shown with the solid black line.

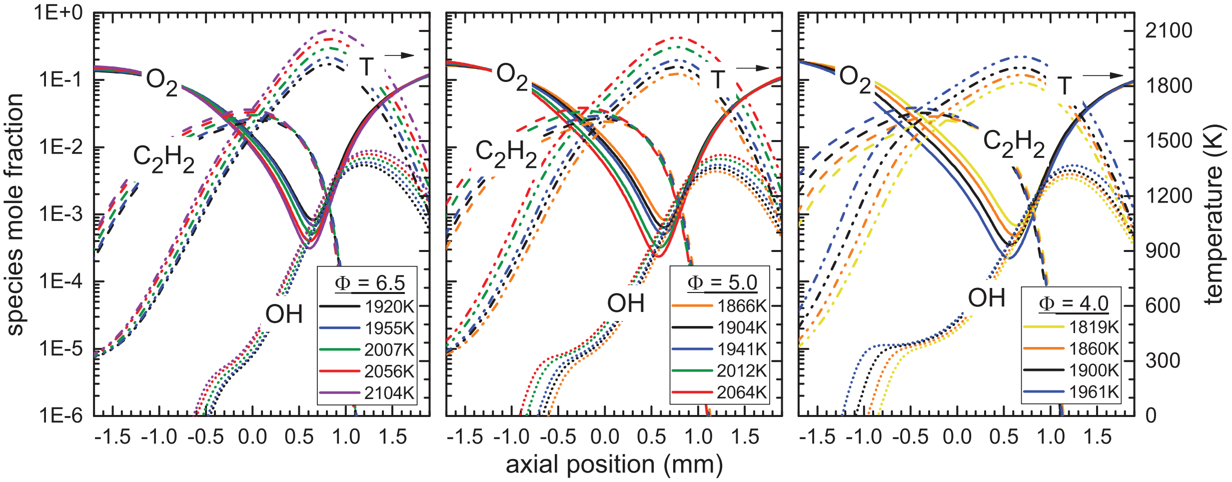

Fig. 3. Computed profiles of temperature and critical soot surface reacting species: OH, O_2, and C_2H_2.

speed of the premixed flame component affects the width of the temperature profile but is difficult to predict accurately. Fig. 4 shows results at each Φ under the non-sooting flame conditions (italic entries) in Table 1. The measured scattering coefficient profiles agree very well with those computed by relying on the gas phase composition and temperature predicted by the model. The comparison shows that the model accurately predicts the profile of Q_{vv}^{gas} resulting from the convolution of temperature and concentration of major scattering species in all the non-sooting flame conditions and that there are no significant artifacts due to beam steering. One would expect that the prediction of the model remains accurate for small changes from the particular values of T_{max} because the implemented perturbation of the flame boundary conditions is small. This is particularly true for the portion of the profile on the oxidizer side of the GSP that, as shown in Fig. 2 and further discussed below, is the zone of the flame where the bulk of soot is formed. For larger deviations of T_{max} from the flames shown in Fig. 2, the soot scattering signal dominates over the gas phase such that any potential uncertainty in the computed Q_{vv}^{gas} or flame width does not affect significantly the inferred soot particle size and number concentration. Potential issues with the model in predicting the laminar flame speed and, consequently, the temperature profile for the flames with largest T_{max} and lowest Φ, may influence the soot volume fractions and dispersion exponent mea-

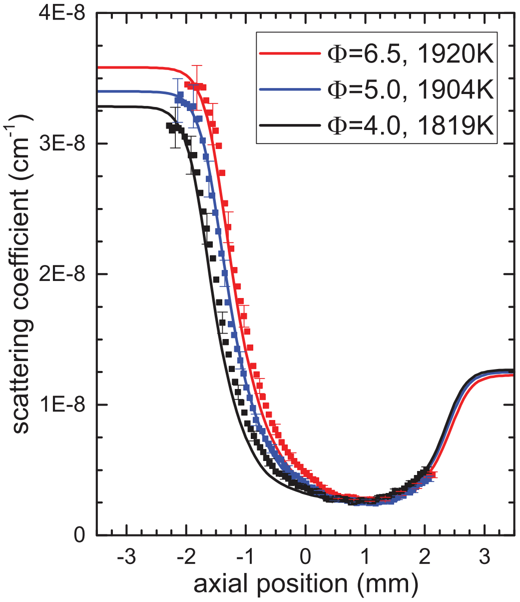

Fig. 4. Computed and measured scattering coefficient of non-sooting flames at three equivalence ratios.

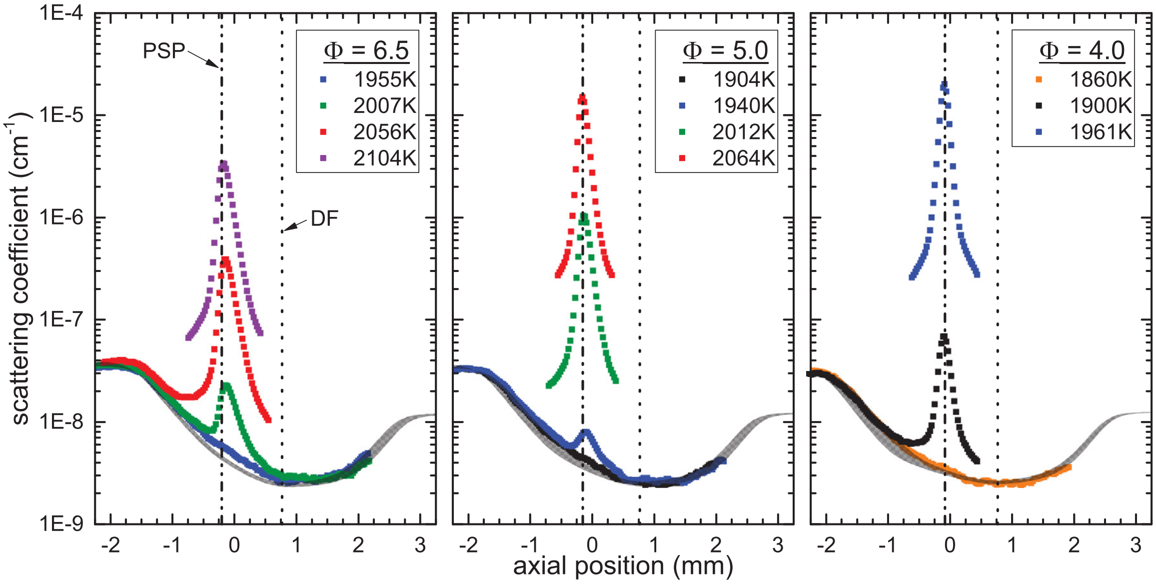

Fig. 5. Measured scattering coefficient of sooting flames. The continuous gray-shaded band at the bottom of the plots represents the computed scattering coefficient of the gas phase for the flames at all investigated T_{max}.

sured on the fuel side of the PSP via pyrometry, but such an effect appears to be insignificant, if present at all, in the context of the ensuing discussion.

3.2. Soot volume fraction, dispersion exponent, and particle size

Before examining derived soot properties, it is useful to look at the “primitive” measured variables such as the scattering coefficient (Q_{vv}), taken as the radial average of 10 pixels (approximately 250 µm) in the proximity of the burner axis at each axial position, and shown in Fig. 5. The gray-shaded band represents the calculated gas-phase scattering contribution, Q_{vv}^{gas}, for the flames at all values of investigated $T_{max.}$ As done with the gaseous species in Fig. 2, the results of the model and experiments are overlapped by superimposing the location of the computed maximum concentration of CH* with that of the maximum chemiluminescence signal of the diffusion flame component in the recorded images. Despite a change in the flame temperature up to approximately 200 K, the value of Q_{vv}^{gas} in the region between the PSP and DF is marginally affected by T_{max}, as indicated by the thickness of the gray shaded region in Fig. 5. One can observe a progressively more apparent (but still minor) broadening of the profile (i.e., thickening of the shaded gray area) on the fuel side of the GSP when decreasing Φ, because of the effect of T_{max} on the laminar flame speed and, consequently, temperature profile thickness. The overlapped experimental data are in good agreement with the calculated Q_{vv}^{gas} in regions devoid of soot. Therefore, the difference between the measured Q_{vv} and Q_{vv}^{gas} can be attributed confidently to soot. The experimental data is truncated for all investigated flames when either the scattered signal is within 10% of the background noise or the finite dynamic range of the intensified camera makes it impossible to quantify Q_{vv}^{gas} in the region devoid of soot. Q_{vv} can span, in fact, up to four orders of magnitude in the sooting containing zone for the flames at the highest T_{max} and lowest Φ. Nevertheless, the majority of the soot-forming region can be characterized also under the heaviest sooting conditions. Note that the accuracy of the model to predict the effect of T_{max} on the laminar flame speed of the PF component does not affect the inferred soot properties. The model has been validated at low T_{max} with the data in Fig. 4 and Q_{vv}^{gas} becomes negligible (less than 1% of the measured scattering signal) compared to that of the excess scattering from soot particles at higher T_{max}. As a result, it is not critical to validate the accuracy of the computed Q_{vv}^{gas} in the moderately sooting flames (e.g., $T_{max} > 2000$ K at $\Phi = 5.0$).

Unsurprisingly, the unequivocal observation emerging from Fig. 5 is that soot is formed on both sides of the PSP. The light scattering measurements complemented by the pyrometry-based determination of the volume fraction allow for an assessment of the relative contributions to soot of the two components of the PPF, with potential uncertainty in the vicinity of the PSP (e.g., size-dependent Brownian diffusion effects) where the two soot domains interface.

Profiles of soot volume fraction and dispersion exponent measured via pyrometry are shown in Fig. 6. Vertical lines mark the position of the Diffusion Flame (DF) component and PSP. The DF component is positioned on the oxidizer side of the GSP and fixed at $z \approx 0.77$ mm for all investigated flames. The position of the PSP shifts slightly closer to the GSP as Φ is lowered because of the progressively milder temperature gradient (see Fig. 3) in the region straddling the GSP, but is almost unaffected by changes in T_{max} at a fixed Φ. The position of the premixed flame (PF) component could not be determined via flame imaging but was inferred from the computed heat release rate and CH* profiles to be between −0.2 mm and −0.9 mm (Fig. 2), depending on T_{max} and Φ. The PF gets closer to the fuel nozzle (i.e., at a more negative value of the abscissa) as either Φ is lowered or T_{max} is increased because of the attending increase in laminar flame speed.

The range of soot volume fraction that can be reliably measured in our experiments is limited either by the need to keep soot at modest levels to neglect soot radiative losses in the computation of the temperature profile or by the lower detection limit of the technique that limits the minimum temperature at which soot is detectable to approximately 1450 K in the current investigated flames. Therefore, fewer data are shown on the premixed side as compared to the scattering data in Fig. 5. For all flames, soot nucleates downstream of the DF, where the flame temperature is maximum, with large values of the dispersion exponent (large H/C). The temperature monotonically decreases as the flame products are convected toward the PSP while the soot volume fraction increases and the dispersion exponent, α, decreases, as particles undergo growth and dehydrogenation. At the lowest values of T_{max}, the trend is reversed before soot reaches the PSP, as the

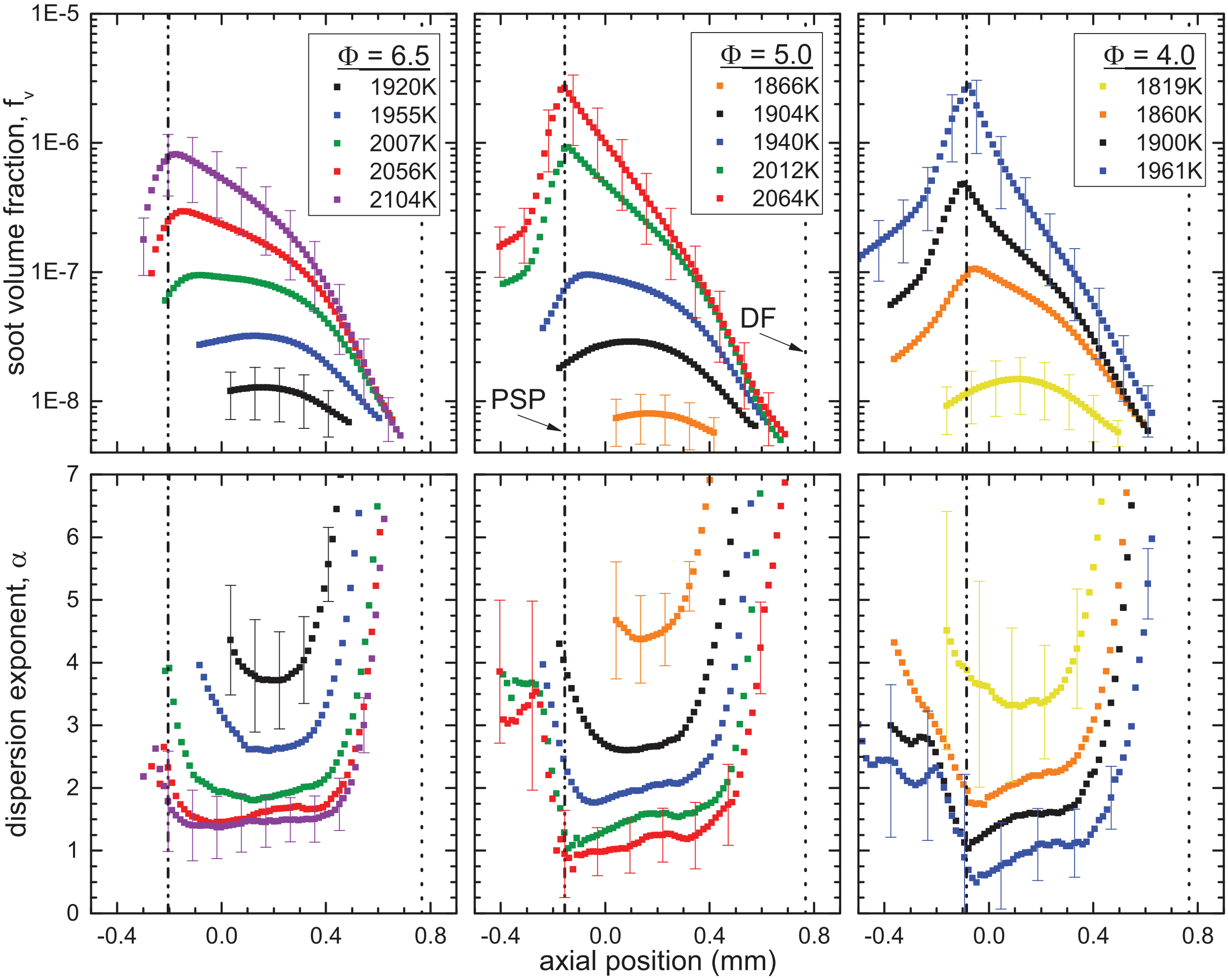

Fig. 6. Measured profiles of soot volume fraction (top) and dispersion exponent (bottom). The abscissa is the axial position with the origin at the GSP, negative values in the fuel stream and positive values in the oxidizer one. The vertical lines mark the position of the diffusion flame (DF) component on the right and of the PSP on the left.

volume fraction begins to decrease while the dispersion exponent increases slightly. The reason for the reversal is the occurrence of soot oxidation from molecular oxygen that is abundant in this zone of the flame, whereas OH is present in concentrations that are too low to play a role (see Fig. 3). The oxidative surface reactions cause a decrease in volume fraction and an increase in the dispersion exponent which is inversely related to soot hydrogen content and maturity [38]. The apparent “de-aging” of soot particles caused by oxidation is unexpected. The increase in α may be due to a change in the particle size affecting the optical properties via quantum confinement effects [50].

The prevalence of oxidation over nucleation/growth in the proximity of the PSP of the flames with the lowest T_{max} causes the appearance of a maximum in the soot volume fraction (minimum in α) that is positioned to the right of the PSP. The shift in the position of these maxima in the profiles suggests greater sensitivity to T_{max} of soot formation as compared to its oxidation. Soot formation dominates clearly over oxidation for the flames at the highest T_{max} in which the maximum volume fraction is positioned at the PSP where the formed particles are convected away radially. The continuous increase in volume fraction moving from the DF toward the PSP, coupled with a gradually decreasing dispersion exponent, suggests that particles undergo continuous aging and dehydrogenation (e.g., through HACA surface growth).

On the premixed flame side of the soot laden region, the interpretation of the results is clearest at the lowest equivalence ratio, Φ=4, where the profiles are to some extent the mirror image of those on the DF side. Soot forms in the post-PF region and grows monotonically towards the PSP with the dispersion coefficient nearly monotonically decreasing as the particle age. The situation is progressively less clear-cut at higher equivalence ratios, with too few data recovered on the PF side, especially at Φ=6.5, to evidence the expected trend. The laser scattering data in Fig. 5 indicate that there is soot formed on the PF side even at Φ=6.5, but the low temperatures limit the quantification of soot volume fraction in these flames.

The measured number concentration and diameter of soot particles are shown in Fig. 7. Data for the lowest T_{max} are not shown because the difference between the measured scattering coefficient and the computed Q_{vv}^{gas} is within the noise limit, so that the scattering contributions from soot particles cannot be quantified. As soot nucleates near the DF, there is an initial increase in number concentration followed by a decrease in the proximity of the PSP, as particle coagulation dominates over nucleation. Despite a consistent factor of two or three increase in volume fraction as T_{max} increases by approximately 50 K, the number concentration is nearly constant in the sooting flame with the lowest T_{max} at Φ = 6.5 and Φ =5.0. Therefore, the small change in T_{max} does not affect preferentially the soot nucleation rate but boosts soot

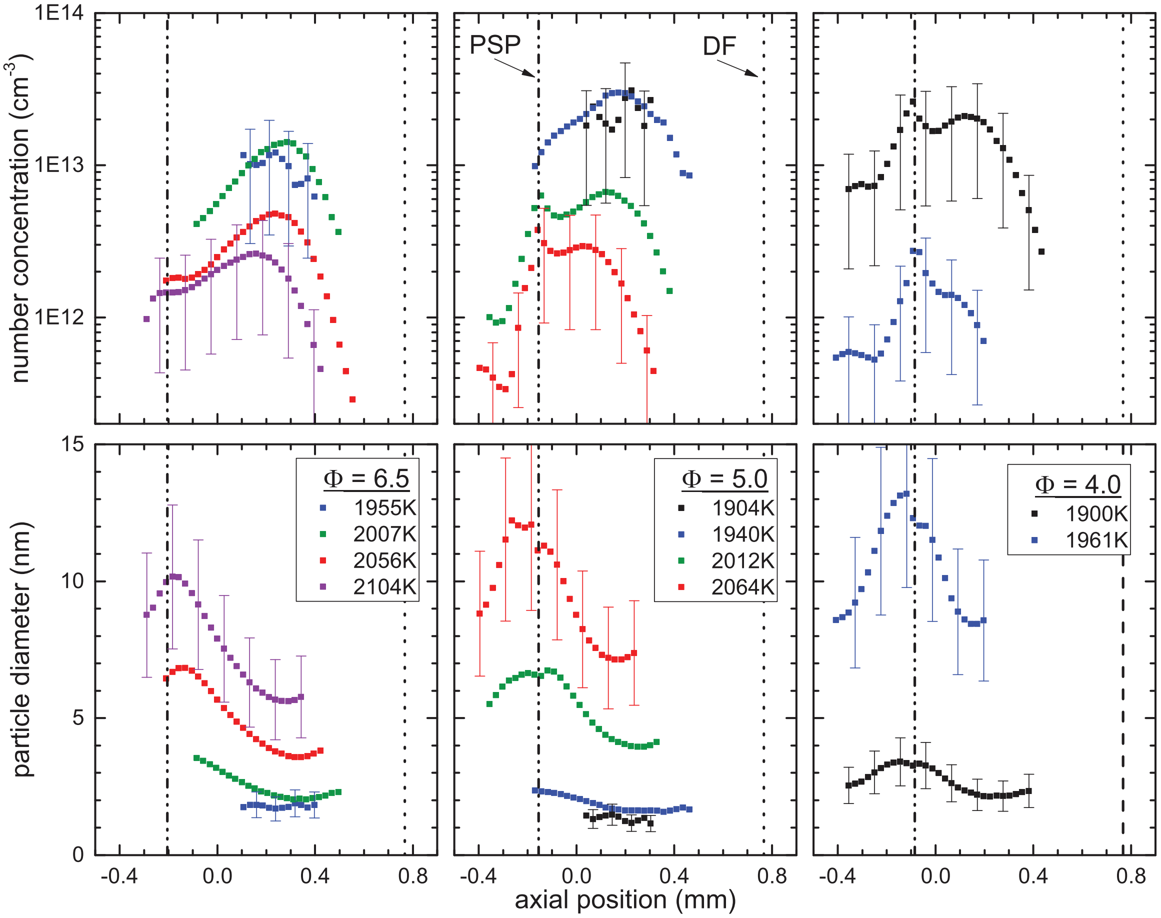

Fig. 7. Profiles of (top) measured soot number concentration and (bottom) measured soot particle diameter by assuming monodisperse distribution.

growth, causing an increase in particle size (in the 1–2 nm range) that contributes to the initial increase in volume fraction. At progressively higher T_{max}, soot particle sizes increase monotonically while soot is convected toward the PSP and particle coagulation becomes increasingly more dominant as highlighted by the systematic decrease in number concentration. As Φ is lowered, the particle sizes increase and exhibit a greater sensitivity to T_{max}, but the maximum number concentration remains on the order of 10^{13}, a value consistent also with that measured in counterflow diffusion flames at atmospheric pressure [49]. The strong sensitivity of particle sizes to Φ can be rationalized on the basis of the shift of the PF component toward the fuel nozzle. This shift not only increases the temperature straddling the GSP, boosting Arrhenius-based (e.g., surface growth) reactions on the DF side of the PSP, but also decreases the oxygen concentration in the soot forming region and partially hinders soot oxidation. The data for Φ=4 reflect a more specular behavior of the DF side and the PF side, with nearly monotonic growth of both number concentration and diameter towards the PSP from both sides.

3.3. Soot production rate

A net soot production rate in terms of either mass or number concentrations can be extracted from the measured volume fraction by writing the soot mass/number balance equation considering both thermophoretic and Brownian effects:

$$\dot{\omega}_s - \dot{\omega}_{s,\,coag} = \frac{d}{dz}\left(\rho Y_s (V_{ax} + V_{th} + V_P)\right) + \rho Y_s \frac{dV_r}{dr}, \tag{6}$$

In Eq. (6), ρ and dV_r/dr are the gas density and radial gradient of the radial velocity computed with the 1-D model, Y_s is either the number concentration or the mass fraction of soot, the latter computed as $Y_s = \rho_s f_v/\rho$ using an assumed soot density ρ_s=1.5 g/cm^3 and the measured soot volume fraction in Fig. 5 from Eq. (2). The term due to coagulation, $\dot{\omega}_{s,\,coag}$, is non-zero only when considering the production rate in terms of number concentrations; details about the method to calculate it are reported elsewhere [26]. The Brownian velocity is estimated by $V_P = -D_P \cdot d\ln(Y_s)/dz$. The value of the Brownian diffusivity is calculated as a function of the measured particle diameter d by

$$D_P = \left(\frac{k_B T}{3\pi \rho_s \nu d}\right)\left[1 + 2Kn\left(A + B\, e^{-\frac{C}{Kn}}\right)\right], \tag{7}$$

with the Knudsen number, Kn, being the ratio of gas mean free path to particle diameter, and A, B, and C empirical constants set equal to 1.257, 0.4, and 0.55, respectively [51]. Since the residence time approaches infinity at the PSP, Eq. (6) is discretized using upwind finite differences for the fuel and oxidizer streams individually, moving toward the PSP from each burner nozzle.

The soot production rate computed using Eq. (6) is shown in Fig. 8. The lack of data near the DF is due to the lack of particle size data that are necessary to quantify the Brownian diffusion contribution. Nevertheless, there are clear trends to infer the effect of T_{max} and Φ on soot formation in PPFs. The soot production rate increases with both an increase in T_{max} and a decrease in Φ. The effects of partial premixing are consistent with the trend reported in [7,15] but in contrast with the findings of [9,12]. As mentioned earlier, since the investigated flames are at constant stoichiometric mixture fraction, the location of the diffusion flame component, which influences the sensitivity to partial premixing [11,12], is fixed, thereby isolating the effects of partial premixing on soot

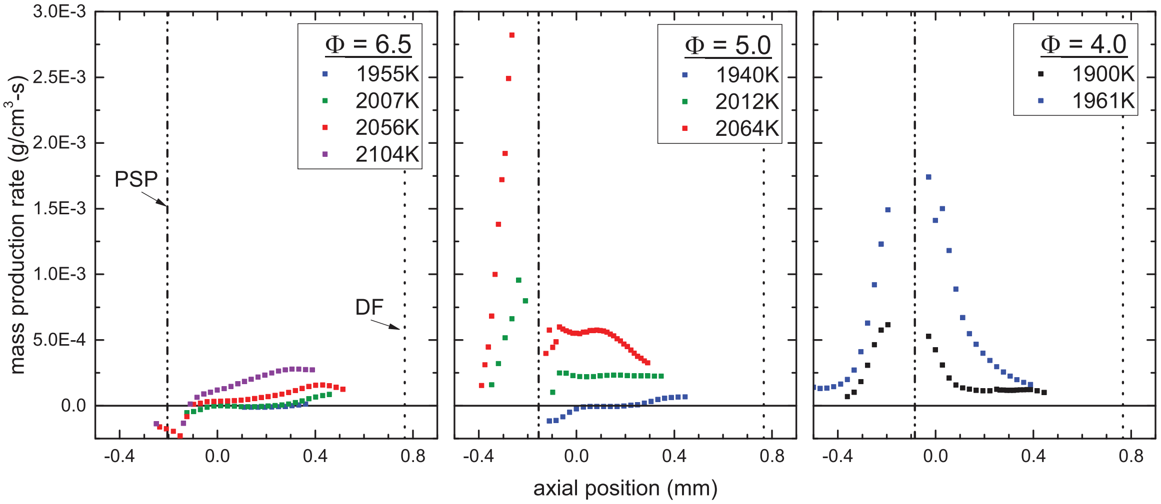

Fig. 8. Calculated net mass production rate of soot based on the experimentally measured volume fraction.

formation. At $\Phi=6.5$, the soot production rate reaches a local maximum at approximately $z=0.4$ mm and decreases in the proximity of the PSP, as Arrhenius-type surface growth reactions are slowed by the lower local temperature and surface oxidation is boosted by larger O_2 concentrations (see Figs. 2 and 3), eventually resulting in a net negative mass production. The prevalence of oxidation is progressively reduced with increasing T_{max} and the T_{max} necessary to avoid net soot consumption by oxidation is reduced when decreasing Φ. The reduced ability of soot oxidation to overtake soot growth in the flames at low Φ occurs because the PF component moves away from the PSP as Φ is lowered, resulting in an overall decrease in the O_2 concentration and an increase in both temperature and C_2H_2 concentration in the region of the flame straddling the GSP where soot formation occurs (see Fig. 3).

As in previous figures, the case of $\Phi=4$ is a bit different, revealing only the positive mass production rate with roughly specular behavior on either side of the PSP. Integrating Eq. (6) along the traverse direction from the nozzle to the PSP provides the soot production rate per unit flame surface area and provides a quantitative way to compare the individual contribution of the DF and PF to the flames overall soot load. In the two highest T_{max} flames at both $\Phi=4$ and $\Phi=5$, the contributions from the PF are within 25% of that of the DF.

To clarify further the observed effect of T_{max} and Φ in Fig. 8, we look specifically at surface growth/oxidation kinetics. Surface growth is modeled by acetylene addition [52,53], by assuming a steric factor (i.e., the probability of successful chemisorption) of 0.7, which is consistent with the values used in [52,54]. Oxidation by OH is assumed to have a collision frequency of 0.13 [55], whereas oxidation by O_2 is based on an empirically derived expression [56] and a temperature-dependent correction factor [57]. The surface growth/oxidation volumetric production rates are calculated by multiplying the surface growth/oxidation kinetic expressions by the total particle surface area per unit volume, S·N, where $S=\pi/4\cdot d^2$ is the surface area of a spherical particle with the measured diameter, d, and N is the measured number concentration. The monodisperse approximation is expected to cause a slight underestimation of the total soot surface area in the investigated conditions, but the accuracy of the estimates affects equally oxidation and surface growth reactions in each of the considered flames. For clarity of presentation, the net computed surface growth rate is presented in Fig. 9 only for the flames with the highest and the lowest T_{max} at each Φ, with these limits bracketing the trends at intermediate temperatures. The shaded bands reflect the uncertainty in two different O_2-oxidation expressions and are bound by a dashed line based on [56] and a solid line based on [57]. For simplicity, we neglect the uncertainty of the assumed steric factor and collision frequency, which should not affect severely the qualitative shape of the computed profiles. Oxidation by OH dominates near the DF component, whereas oxidation by O_2 dominates near the PSP where the OH concentration is low (see Figs. 2 and 3). However, since the particle surface area per unit volume is smallest near the DF and largest near the PSP, it is primarily O_2 that contributes to the overall net consumption of soot in the investigated PPFs.

Results in Fig. 9 are consistent with those in Fig. 8. The occurrence of negative surface growth supports the observed negative production rate near the PSP. The rate of surface growth initially increases approaching the PSP from the DF, as C_2H_2 concentration increases, but reaches a maximum and decreases as temperature decreases and O_2 concentration increases. Oxidation by O_2 appears to dominate the region straddling the PSP at all Φs, but the uncertainty in the existing O_2 oxidation models (note the difference between the two tested ones) makes it impossible to assess whether either O_2 oxidation or C_2H_2 growth dominates at a specific location in each of the considered flames. Overall, the concentration of O_2 and C_2H_2 decreases and increases as T_{max} increases and Φ decreases, respectively (see Fig. 3), both resulting in the net positive increase in surface growth that is observed in Fig. 8. These trends indicate that a non-monotonic behavior between partial premixing and soot emissions is possible at sufficiently high equivalence ratios ($\Phi>6.5$), similar to the trends reported in past studies [12]. At $\Phi=4.0$, the surface growth is predicted to be negative on the left of the PSP, indicating that the PF component may nucleate particles persistently downstream of the flame front when the net mass soot production is measured to be positive (Fig. 8). The results suggest that this persistent nucleation in the PF occurs at temperatures (<1700 K) which are sufficiently low to inhibit both surface growth and high-temperature inception and is dominated by a mechanism involving PAHs [22,58].

All in all, soot nucleation remains the most challenging process to be quantitatively described. This is partly due to the fact that the experimental tracking of gas-to-particle transition is very difficult, especially so if spatial resolution has to be retained. The discrepancy between state-of-the-art model predictions of soot load and experimental results in Fig. 2, even though simple soot oxidation and surface growth describe reasonably well the experimental results in Figs. 8 and 9, at least for $\Phi=6.5$ and

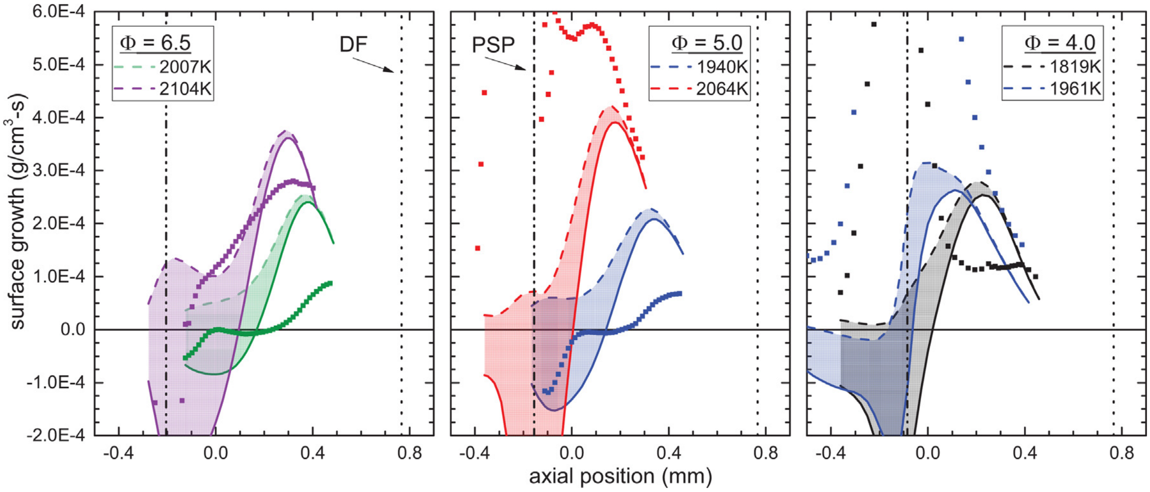

Fig. 9. Net soot surface growth rates by C_2H_2, OH, and O_2. Shaded bands reflect the uncertainty associated with different empirical O_2-oxidation models and are bound by upper dashed lines based on the expression in [57] and lower solid lines based on that in [56]. Symbols are the experimentally measured net mass production rate from Fig. 7.

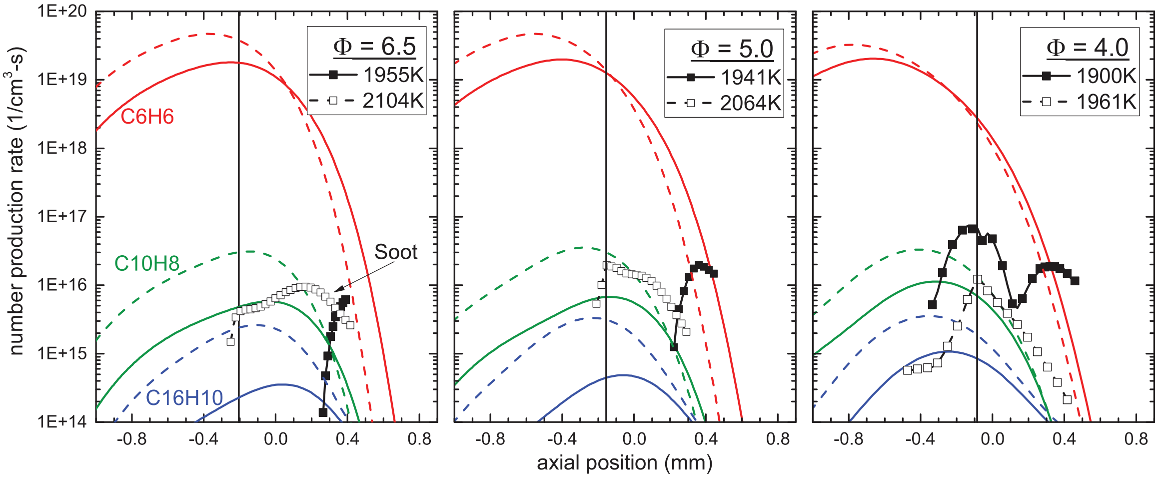

Fig. 10. Profiles of soot nucleation rate inferred from experiments and modeled dimerization rate of several PAHs assuming 1% collision efficiency. The vertical line marks the position of the PSP.

Φ=5.0, suggests that something is amiss also on the modeling side.

To complement the analysis of surface growth and oxidation, we analyze further the nucleation step in Fig. 10 by comparing the soot *number* production rate inferred from experiments to the dimerization rate of benzene (C_6H_6), naphthalene ($C_{10}H_8$), and pyrene ($C_{16}H_{10}$) for two values of T_{max}. Full symbols and solid lines represent the lowest considered T_{max} and open symbols and dashed lines represent the highest considered T_{max}. The method used to evaluate dimerization rates from the validated concentrations [26] is based on the kinetic theory collision rate considering a 1% dimerization probability upon self-collision of aromatic species. Only the smallest aromatics are present in flames at sufficiently large concentrations to account for soot nucleation. This finding is consistent with a similar one in purely diffusion flames at several pressures [26,49]. While we have assumed a comparatively large probability for the sticking probability, we find that naphthalene dimerization can provide a reasonable estimate for soot nucleation as proposed in simplified kinetic models [59], particularly at higher T_{max} and lower Φ. However, it remains a challenge for chemistry mechanisms to predict accurately benzene and naphthalene for a wide range of experimental flame conditions [7,15,24,32] while also trying to predict larger species such as pyrene and coronene. PAHs are more abundant in the region on the fuel side of the GSP, so that progressively larger aromatics may contribute to nucleation from the premixed flame component, especially for the flames at the highest T_{max} in which even the estimated dimerization of pyrene can match the measured soot nucleation rate. However, it appears that the finding that small aromatics control soot nucleation applies also to soot formed from the PF component in flames at low T_{max}. This is particularly true if one considers that the dimerization probability of small PAHs is likely much smaller than the assumed 1% and that the experimental data analysis may significantly underestimate the number production rate for the flames at the highest T_{max} because of the assumed monodispersity of the soot particle population.

Conclusions

We report on the effect of temperature and equivalence ratio on soot formation in atmospheric pressure counterflow partially premixed flames (PPFs) of ethylene at equivalence ratios, Φ, equal to 6.5, 5.0, and 4.0. Principal conclusions follow.

- At fixed Φ, raising the peak temperature invariably raises the soot volume fraction throughout the soot laden region sandwiched between the two flame components and promotes soot formation from both the diffusion flame component and the premixed flame component.

- The region on the oxidizer side between the diffusion flame component and the particle stagnation plane reveals the typical scenario of a purely diffusive flame: soot nucleates downstream of the diffusion flame, with large values of the dispersion exponent (large H/C). As the flame products are convected toward the particle stagnation plane (PSP), soot volume fraction increases and the dispersion exponent decreases, as particles undergo growth and dehydrogenation.
- Except for the highest temperatures, when soot continues to grow until reaching the PSP, the volume fraction begins to decrease before the PSP while the dispersion exponent increases slightly. This reversal is attributed to soot oxidation from molecular oxygen diffusing near the GSP from the premixed component of the flame. Under these conditions, the net soot production rate turns negative locally, with surface oxidation prevailing on surface growth.
- As the equivalence ratio is lowered, the premixed flame component shifts away from the diffusion flame component. The resulting broadening and local temperature increase of the soot forming region promotes soot formation, as surface growth is enhanced and oxidation is suppressed because of the lower concentration of O_2, resulting in the increase of both soot volume fraction and particle sizes.
- Comparing the soot *number* production rate inferred from experiments to the dimerization rate of benzene (C_6H_6), naphthalene ($C_{10}H_8$), and pyrene ($C_{16}H_{10}$) reveals that only the smallest aromatics are present in flames at sufficiently large concentrations to account for soot nucleation. This observation applies to both the diffusion flame and the premixed flame components.

Declaration of Competing Interest

The authors declare that they have no known competing financial interests or personal relationships that could have appeared to influence the work reported in this paper.

Acknowledgments

K.G. and A.G. acknowledge the support of the National Science Foundation (CBET-1853150). Authors declare no competing interests.

References

[1] B.S. Haynes, H.G. Wagner, Soot formation, Prog. Energy Combust. Sci. 7 (1981) 229–273.
[2] Y. Wang, S.H. Chung, Soot formation in laminar counterflow flames, Prog. Energy Combust. Sci. 74 (2019) 152–238.
[3] H. Wang, Formation of nascent soot and other condensed-phase materials in flames, Proc. Combust. Inst. 33 (2011) 41–67.
[4] J.E. Dec, Advanced compression-ignition engines—Understanding the in-cylinder processes, Proc. Combust. Inst. 32 (2009) 2727–2742.
[5] B. Frank, R. Schlogl, D.S. Su, Diesel soot toxification, Environ. Sci. Technol. 47 (2013) 3026–3027.
[6] T.C. Bond, S.J. Doherty, D.W. Fahey, et al., Bounding the role of black carbon in the climate system: a scientific assessment, J. Geophys. Res. Atmos. 118 (2013) 5380–5552.
[7] F. Carbone, F. Cattaneo, A. Gomez, Structure of incipiently sooting partially premixed ethylene counterflow flames, Combust. Flame. 162 (2015) 4138–4148.
[8] Y. Hua, L. Qiu, F. Liu, Y. Qian, S. Meng, Numerical investigation into the effects of oxygen concentration on flame characteristics and soot formation in diffusion and partially premixed flames, Fuel 268 (2020) 117398.
[9] P. Berta, S.K. Aggarwal, I.K. Puri, An experimental and numerical investigation of n-heptane/air counterflow partially premixed flames and emission of NOx and PAH species, Combust. Flame. 145 (2006) 740–764.
[10] S.C. Li, F.A. Williams, Counterflow heptane flame structure, Proc. Combust. Inst. 28 (2000) 1031–1038.
[11] H.P. Mungekar, A. Atreya, Flame Radiation and Soot Emission From Partially Premixed Methane Counterflow Flames, J. Heat Transfer. 128 (2006) 361.
[12] H.P. Mungekar, A. Atreya, Effect of partial premixing on the sooting structure of methane flames, Combust. Flame. 144 (2006) 336–348.
[13] J.Y. Hwang, S.H. Chung, W. Lee, Effects of oxygen and propane addition on soot formation in counterflow ethylene flames and the role of C3 chemistry, Symp. Combust. 27 (1998) 1531–1538.
[14] S. Liang, Z. Li, J. Gao, X. Ma, H. Xu, S. Shuai, PAHs and soot formation in laminar partially premixed co-flow flames fuelled by PRFs at elevated pressures, Combust. Flame. 206 (2019) 363–378.
[15] F. Carbone, K. Gleason, A. Gomez, Pressure effects on incipiently sooting partially premixed counterflow flames of ethylene, Proc. Combust. Inst. 36 (2017) 1395–1402.
[16] A.K. Makwana, S. Iyer, M. Linevsky, R. Santoro, T. Litzinger, J. O'Connor, Effect of aromatic fuels and premixing on aromatic species and soot distributions in laminar, co-flow flames at atmospheric pressure, Combust. Flame. 194 (2018) 164–174.
[17] L. Xu, F. Yan, M. Zhou, Y. Wang, An experimental and modeling study on sooting characteristics of laminar counterflow diffusion flames with partial premixing, Energy 218 (2021) 119479.
[18] X. Fu, X. Han, K. Brezinsky, S.K. Aggarwal, Effect of fuel molecular structure and premixing on soot emissions from n-heptane and 1-heptene flames, Energy Fuels 27 (2013) 6262–6272.
[19] X. Han, S.K. Aggarwal, K. Brezinsky, Effect of unsaturated bond on NOx and PAH formation in n-heptane and 1-heptene triple flames, Energy Fuels 27 (2013) 537–548.
[20] I. Glassman, P. Yaccarino, The temperature effect in sooting diffusion flames, Proc. Combust. Inst. 18 (1981) 1175–1183.
[21] R.L. Axelbaum, W.L. Flower, C.K. Law, Dilution and temperature effects of inert addition on soot formation in counterflow diffusion flames, Combust. Sci. Technol. 61 (1988) 51–73.
[22] K. Gleason, F. Carbone, A. Gomez, Effect of temperature on soot inception in highly controlled counterflow ethylene diffusion flames, Combust. Flame. 192 (2018) 283–294.
[23] A. Ciajolo, A. D'Anna, R. Barbella, A. Tregrossi, A. Violi, The effect of temperature on soot inception in premixed ethylene flames, Proc. Combust. Inst. 26 (1996) 2327–2333.
[24] S. Dasappa, J. Camacho, Evolution in size and structural order for incipient soot formed at flame temperatures greater than 2100K, Fuel 291 (2021) 120196.
[25] H. Liu, Y. Cui, B. Chen, D.C. Kyritsis, Q. Tang, L. Feng, Y. Wang, Z. Li, C. Geng, M. Yao, Effects of flame temperature on PAHs and soot evolution in partially premixed and diffusion flames of a diesel surrogate, Energy Fuels 33 (2019) 11821–11829.
[26] K. Gleason, F. Carbone, A.J. Sumner, B.D. Drollette, D.L. Plata, A. Gomez, Small aromatic hydrocarbons control the onset of soot nucleation, Combust. Flame. 223 (2021) 398–406.
[27] K. Gleason, F. Carbone, A. Gomez, Pressure and temperature dependence of soot in highly controlled counterflow ethylene diffusion flames, Proc. Combust. Inst. 37 (2019) 2057–2064.
[28] L. Figura, F. Carbone, A. Gomez, Challenges and artifacts of probing high-pressure counterflow laminar diffusion flames, Proc. Combust. Inst. 35 (2015) 1871–1878.
[29] A.N.S.Y.S. CHEMKIN-Pro Release 2019 R2.
[30] E. Ranzi, C. Cavallotti, A. Cuoci, A. Frassoldati, M. Pelucchi, T. Faravelli, New reaction classes in the kinetic modeling of low temperature oxidation of n-alkanes, Combust. Flame. 162 (2015) 1679–1691.
[31] CRECK C1-C16 high temperature soot (HT+SOOT) mechanism: http://creckmodeling.chem.polimi.it/menu-kinetics/menu-kinetics-detailed-mechanisms/107-category-kinetic-mechanisms/411-mechanisms-1911-tot-ht-soot.
[32] W. Pejpichestakul, A. Cuoci, A. Frassoldati, M. Pelucchi, A. Parente, T. Faravelli, Buoyancy effect in sooting laminar premixed ethylene flame, Combust. Flame. 205 (2019) 135–146.
[33] W.L. Grosshandler, RADCAL: a narrow-band model for radiation calculations in a combustion environment., NIST Tech. Note 1402. (1993) 52.
[34] W.H. Dalzell, A.F. Sarofim, Optical constants of soot and their application to heat-flux calculations, J. Heat Transfer. 91 (1969) 100–104.
[35] P.B. Kuhn, B. Ma, B.C. Connelly, M.D. Smooke, M.B. Long, Soot and thin-filament pyrometry using a color digital camera, Proc. Combust. Inst. 33 (2011) 743–750.
[36] F. Carbone, K. Gleason, A. Gomez, Probing gas-to-particle transition in a moderately sooting atmospheric pressure ethylene/air laminar premixed flame. Part I: gas phase and soot ensemble characterization, Combust. Flame. 181 (2017) 315–328.
[37] J. Simonsson, N.E. Olofsson, T. Sandra, P.E. Bengtsson, H. Bladh, Wavelength dependence of extinction in sooting flat premixed flames in the visible and near-infrared regimes, Appl. Phys. B Lasers Opt. 119 (2015) 657–667.
[38] H.A. Michelsen, Effects of maturity and temperature on soot density and specific heat, Proc. Combust. Inst. 38 (2021) 1197–1205.
[39] F. Cignoli, S. De Iuliis, V. Manta, G. Zizak, Two-dimensional two-wavelength emission technique for soot diagnostics, Appl. Opt. 40 (2001) 5370–5378.
[40] B. Ma, M.B. Long, Absolute light calibration using S-type thermocouples, Proc. Combust. Inst. 34 (2013) 3531–3539.
[41] C. Schulz, B.F. Kock, M. Hofmann, H.A. Michelsen, S. Will, B. Bougie, R. Suntz, G.J. Smallwood, Laser-induced incandescence: recent trends and current questions, Appl. Phys. B. 83 (2006) 333–354.
[42] C.J. Dasch, Continuous-wave probe laser investigation of laser vaporization of small soot particles in a flame, Appl. Opt. 23 (1984) 2209.

[43] J.A. Sutton, J.F. Driscoll, Rayleigh scattering cross sections of combustion species at 266, 355, and 532nm for thermometry applications, Opt. Lett. 29 (2004) 2620–2622.
[44] G. Sutton, A. Levick, G. Edwards, D. Greenhalgh, A combustion temperature and species standard for the calibration of laser diagnostic techniques, Combust. Flame. 147 (2006) 39–48.
[45] A. D'Alessio, Laser light scattering and fluorescence diagnostics of rich flames produced by gaseous and liquid fuels, in: D.C. Siegla (Ed.), Part. Carbon, Springer (1981), pp. 207–259.
[46] M.P. Bogaard, A.D. Buckingham, R.K. Pierens, A.H. White, Rayleigh scattering depolarization ratio and molecular polarizability anisotropy for gases, J. Chem. Soc. Faraday Trans. 1 Phys. Chem. Condens. Phases. 74 (1978) 3008–3015.
[47] H.A. Michelsen, P.E. Schrader, F. Goulay, Wavelength and temperature dependences of the absorption and scattering cross sections of soot, Carbon N. Y. 48 (2010) 2175–2191.
[48] S.L. Goren, Thermophoresis of aerosol particles in the laminar boundary layer on a flat plate, J. Colloid Interface Sci. 61 (1977) 77–85.
[49] K. Gleason, F. Carbone, A. Gomez, PAHs controlling soot nucleation in 0.101—0.811MPa ethylene counterflow diffusion flames, Combust. Flame. 227 (2021) 384–395.
[50] K. Wan, X. Shi, H. Wang, Quantum confinement and size resolved modeling of electronic and optical properties of small soot particles, Proc. Combust. Inst. 38 (2021) 1517–1524.
[51] S.K. Friedlander, Smoke, Dust and Haze: Fundamentals of Aerosol Behavior, John Wiley & Sons Inc, 1977.
[52] M. Frenklach, H. Wang, Detailed modeling of soot particle nucleation and growth, Proc. Combust. Inst. 23 (1991) 1559–1566.
[53] M. Frenklach, New form for reduced modeling of soot oxidation: accounting for multi-site kinetics and surface reactivity, Combust. Flame. 201 (2019) 148–159.
[54] A. Khosousi, S.B. Dworkin, Soot surface reactivity during surface growth and oxidation in laminar diffusion flames, Combust. Flame. 162 (2015) 4523–4532.
[55] K.G. Neoh, J.B. Howard, A.F. Sarofim, Soot Oxidation in Flames, in: D.C. Siegla (Ed.), Part. Carbon Form. Dur. Combust., Springer (1981), pp. 261–282.
[56] J. Nagle, R.F. Strickland-Constable, Oxidation of Carbon Between 1000-2000C, Proc. Fifth Carbon Conf. 1 (1962) 154.
[57] F. Liu, H. Guo, G.J. Smallwood, Ö.L. Gülder, Numerical modelling of soot formation and oxidation in laminar coflow non-smoking and smoking ethylene diffusion flames, Combust. Theory Model. 7 (2003) 301–315.
[58] H. Guo, Z. Gub, K.A. Thomson, G.J. Smallwood, F.F. Baksh, Soot formation in a laminar ethylene/air diffusion flame at pressures from 1 to 8 atm, Proc. Combust. Inst. 34 (2013) 1795–1802.
[59] F. Bisetti, G. Blanquart, M.E. Mueller, H. Pitsch, On the formation and early evolution of soot in turbulent nonpremixed flames, Combust. Flame. 159 (2012) 317–335.